Synthesis of three-dimensionally ordered macroporous manganese dioxide–carbon nanocomposites for supercapacitors

CrossMark

Zhi Liu*, Xiuli Tan, Xin Gao, Lihong Song

Institute of Chemistry for Functionalized Materials, Faculty of Chemistry and Chemical Engineering, Liaoning Normal University, Dalian 116029, PR China

HIGHLIGHTS

- Three-dimensionally ordered macroporous MnO_2–carbon nanocomposites (3DOM MCNs) are prepared.
- The 3DOM MCNs possess hierarchical pore structure with highly dispersed MnO_2 nanoparticles.
- The 3DOM MCNs are promising for supercapacitor applications.

ARTICLE INFO

ABSTRACT

In this article, we report a composite of MnO_2 nanoparticles supported by three-dimensionally ordered macroporous carbon (MnO_2/3DOM carbon nanocomposites) fabricated by means of a simple multi-component infiltration of three-dimensional templates. MnO_2 nanoparticles of 2 nm–6 nm are observed to be highly dispersed on the 3DOM carbon scaffolds. Cyclic voltammetry, galvanostatic charge/discharge and electrochemical impedance spectroscopy techniques are employed to assess the properties of these nanocomposites for use in supercapacitors. The results demonstrate that MnO_2 can be effectively utilized with assistance of the 3DOM carbon in the electrode. The specific capacitance of the nanocomposite electrode can reach as high as 347 F g^{-1} at a current density of 0.5 A g^{-1}. Moreover, the electrode exhibit excellent charge/discharge rate and good cycling stability, retaining over 92% of its initial charge after 5500 cycles at a current density of 2.5 A g^{-1}. Such MnO_2/3DOM carbon nanocomposite represents a promising exploring direction for enhancing the device performance of metal oxide-based electrochemical supercapacitors.

© 2014 Elsevier B.V. All rights reserved.

1. Introduction

Recently, the interest in the design and fabrication of MnO_2–carbon nanocomposites (MCNs) with various architectures as supercapacitors is growing rapidly owing to their remarkably enhanced capacitive performance compared to the single MnO_2 or carbon counterpart [1,2]. The combination of MnO_2 with carbon not only in principle retains the high theoretical specific capacitance of MnO_2 (1370 F g^{-1}) with significantly improved conductivity, but it also fully utilizes the structural versatility of carbon materials (one, two, or three-dimension) with rich porosities and high accessible surface areas to well disperse the MnO_2 phase. Up to date, various forms of MCNs, such as MnO_2 associating with activated carbon [3,4], carbon nanotubes [5–8], graphene or reduced graphene oxide [9–11], graphite [12,13], carbon cloth [14], ordered mesoporous carbon [15–17], carbon aerogels and nanofoams [18,19], have been

synthesized by different approaches including chemical or electrochemical deposition, redox reaction, sonochemical or microwave-assisted synthesis, and layer by layer assembly. Although desired capacitive enhancements are achieved to some degree, these fabrication techniques are often costly, experimentally fussy with multistep synthesis procedures, time/energy-consuming, and hard to produce in large-scale. Moreover, they uncontrollably either come into being a random distribution of constitutive MnO_2 and carbon phases, or result in the preferential formation of MnO_2 layers located on the exterior of the carbon substrates, which inevitably blocks inwards diffusion of MnO_2 and consequently leads to a low MnO_2 utilization at a high loading content. Even worse, the formed MnO_2 probably decreases pore accessibility of ions and electron conductivity of the MCNs. Therefore, designing a scalable strategy for fabricating a new MCN with a uniform framework composition, the highest possible dispersion of MnO_2 nanostructure with regular pore texture for easy transport of ions as well as good electron conductivity ability,

---

is highly desired and attractive for ensuring a satisfactory capacitance performance.

Over the past years, three-dimensionally ordered macroporous (3DOM) materials, with uniform pore size and well-defined periodic structure, have stimulated much more attention due to their potential applications in electrochemistry, catalysis, separation and photonic crystals, etc [20–22]. Particularly in electrochemistry used as supercapacitors, in addition to their 3D network paths, uniform pore sizes, interconnected macropores providing a fast ion transportation pathway for the electrolyte to reach the surface of the active material, and contribution electrical double-layer capacitance (EDLC) to the overall energy storage, the 3DOM materials with a hierarchical porous texture can generate large specific surface area to increase effective interfacial area between the active phase and the electrolyte, thus maximizing the capacitance. As a continuous network of electrode materials, 3DOM materials are monolithic which have smoother electron conductivity than loosely aggregated nanocrystalline materials. Furthermore, the free space within porous 3D electrodes can act as buffer for the drastically volume variation of the entire electrode during the consecutive charge/discharge process [23–31]. Conventionally, the colloidal crystal templating strategy (CCTS) is employed to prepare 3DOM materials [32]. Briefly, uniform monodispersed microspheres, such as polymethyl methacrylate (PMMA), polystyrene or silica spheres, can assemble into ordered three-dimensional array in densified packing. These ordered arrays offer a 3D scaffold in which a variety of precursors can be infiltrated. After subsequent solidification of the precursors and removal of the colloidal microspheres, periodic 3D framework structures are obtained. To the best of our knowledge, there are scarce reports to date concerning a 3DOM MCN possessing a hierarchical pore structure with a uniform composition of MnO_2 and carbon used as supercapacitors. Aroused by this interest, we for the first time report the synthesis of a novel 3DOM material composed of MnO_2 and carbon by means of a multi-component (manganous nitrate, phenol–formaldehyde resol, and triblock copolymer F127) infiltration of 3D templates. F127 was selected as a structure-directing agent to create mesopores in 3DOM skeletons and increase surface area for charge storage. The resulting MCNs exhibit highly ordered 3D macroporous structures. The MnO_2 content in the MCNs can be continuously tuned from 6.5 to 21.3 wt.%, and MnO_2 nanoparticles are highly distributed on the macropore walls of the 3DOM carbon scaffold. When tested as supercapacitor electrodes, the MCN with a MnO_2 content of 21.3 wt.% exhibits the best capacitive performance with a total specific capacitance of 347 F g^{-1} and a MnO_2 specific capacitance of 1178 F g^{-1} at a current density of 0.5 A g^{-1}.

2. Experimental

2.1. Chemical agents

Pluronic F127 ($EO_{106}PO_{70}EO_{106}$) was supplied by Sigma–Aldrich and has an average molecular weight of 12,600. Methyl methacrylate (MMA), potassium persulfate ($K_2S_2O_8$), $Mn(NO_3)_2$ (50 wt.%) solution and sodium hydroxide (NaOH) were purchased from Tianjin Kermel Chemical Reagent Co. Ltd. Phenol, formaldehyde (37 wt.%), hydrochloric acid (37 wt.%) (HCl), and ethanol were purchased from Shenyang Chemical Preparation Corp. All the chemicals were used as received without further purification. Deionized water was used in all experiments.

2.2. Synthesis of PMMA template

The PMMA colloidal crystal templates for the creation of 3DOM MCN were synthesized via a soap-free-emulsion polymerization according to a modified procedure based on Ref. [33]. In a typical synthesis, a desired amount of monomer MMA was washed three times with a NaOH solution (10 wt.%) and di-distilled water respectively to remove any traces of the inhibitor. Then, 11.3 g of the washed MMA and 150 g of di-distilled water were added to a 500 mL round bottom flask and stirred for a while. Then, 12 mL (0.0005 g mL^{-1}) $K_2S_2O_8$ was added to the solution and the mixture was constantly reacted at 70 °C for 7 h under a nitrogen atmosphere with mild stirring until a milky solution appeared. After filtering the milky solution to remove large agglomerates, the monodispersed PMMA microspheres were obtained. Finally, the as-synthesized monodispersed PMMA microspheres were packed into PMMA colloidal crystal template by evaporating the water solvent at 70 °C for 24 h.

2.3. Preparation of precursors

The phenol–formaldehyde (P–F) resol precursor was prepared according to Ref. [34]. Briefly, 6.0 g of phenol was mixed with 1.0 g of 20 wt.% NaOH aqueous solution under stirring, and 10.0 g of formaldehyde solution was then added. The resulting transparent solution was stirred at 75 °C for 1 h, cooled to room temperature, and the pH was then adjusted to about 7.0 by 2.0 mol L^{-1} HCl. After water was removed by distillation, the mixture was redispersed in a required amount of ethanol. The NaCl precipitate was removed by filtration, and the filtrate, the P–F resol precursor with a concentration of 50 wt.% in ethanol, was collected for further use. For a typical synthesis of manganese precursor (MP), a required amount of $Mn(NO_3)_2$ was dissolved in 11.0 g of ethanol under stirring for 30 min. Next, 1.0 g of P–F resol was added to the solution and stirred for another 1 h. To the above resulting solution was added 0.11 g of F127 and then stirring overnight. By varying the amount of $Mn(NO_3)_2$, the MPs with different content of manganese were prepared and denoted as MP-B, MP-C, and MP-D, respectively. In addition, a blank manganese precursor (denoted as MP-A) was also prepared under the same conditions as those for the MPs, but without the adding of $Mn(NO_3)_2$. The detailed preparation conditions and the corresponding sample I.D. are summarized in Table 1.

2.4. Preparation of 3DOM MCNs

The hierarchical pore structured 3DOM MCN was prepared by employing the CCTS with the different MPs. Typically, the PMMA template was firstly soaked in the MP for 30 min. Care was taken to keep the solution level below the top of the PMMA template. After wiping off the excess solution, the infiltered template was dried at 100 °C for 2 h. Then, the soaking-drying steps were repeated for three times to ensure a complete filling of the void spaces between the PMMA microspheres. Finally, the resultant was pyrolyzed under flowing N_2 at 450 °C for 2 h and then at 800 °C for another 3 h with a heating rate of 1 °C min^{-1}. The as-synthesized products were denoted as A, B, C and D.

2.5. Electrode preparation and electrochemical measurements

The fabrication of working electrodes was carried out as follows. Briefly, the active material (the as-prepared samples A–D), carbon

Table 1
Synthesis conditions of manganese precursor.

MCN sample I.D.	Manganese precursor	$Mn(NO_3)_2$ (50 wt.%) (g)	Ethanol (g)	P–F resol (g)	F127 (g)
A	MP-A	0.0	11.0	1.0	0.11
B	MP-B	0.15	11.0	1.0	0.11
C	MP-C	0.31	11.0	1.0	0.11
D	MP-D	0.54	11.0	1.0	0.11
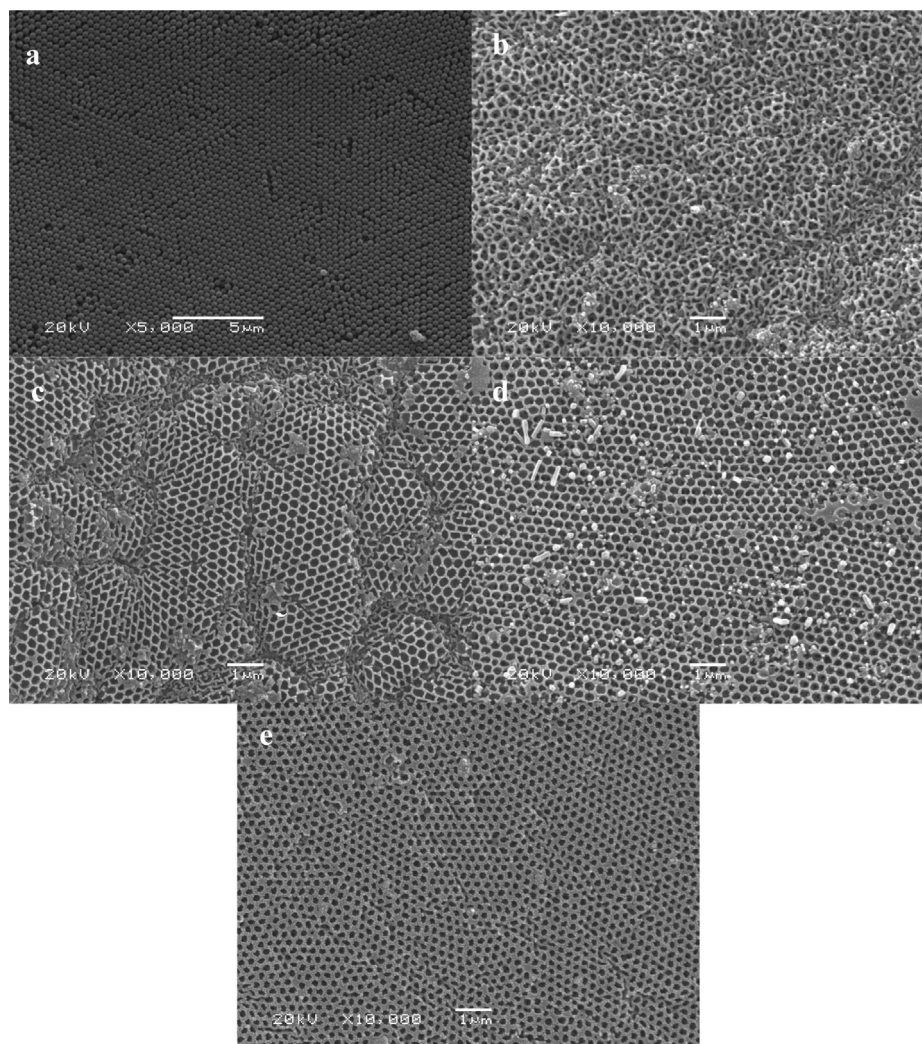
Fig. 1. SEM images of PMMA template (a) and the samples A–D prepared with MP-A (b), MP-B (c), MP-C (d) and MP-D (e).

black and poly(vinylidene fluoride) were mixed in a mass ratio of 85:10:5 and dispersed in ethanol to obtain a homogeneous paste. Then the paste was coated onto the nickel foam (current collector) with an area of 1 cm^2 on each side, and pressed under a pressure of 5 MPa (determined by advance compression optimization) to assure good electrical contact [31]. Finally, the as-prepared electrodes were dried overnight at 100 °C in a vacuum oven. Prior to the electrochemical measurements, the electrodes were impregnated with electrolyte under vacuum for 2 h to reduce air contamination and improve wettability. The Cyclic voltammetry (CV) and galvanostatic charge/discharge (GCD) studies were performed using a Zahner IM6e electrochemical station with a conventional three-electrode electrochemical cell, employing a platinum wire as the counter electrode and a saturated calomel electrode (SCE) as the reference electrode. The electrolyte was 0.1 M Na$_2$SO$_4$ aqueous solution. CV tests were carried out in the potential range between 0 and 0.8 V versus SCE at room temperature (24 °C) at varied scan rates from 5 to 200 mV s^{-1}. GCD measurements were conducted between 0 and 0.8 V at different current densities of 0.5, 1, 2.5, 5, 7.5 and 10 A g^{-1} to calculate the specific capacitances and cycling life of the electrode materials. Electrochemical impedance spectroscopy (EIS) measurements were performed on a Solartron 1287 using a sinusoidal signal with an amplitude of 10 mV in the frequency range from 100 kHz to 10 mHz.

2.6. Characterizations

Scanning electron microscope (SEM) experiments were performed with a JSM 6360-LV electron microscope. The samples were vapor-deposited with gold before observation. X-ray photoelectron spectroscopy (XPS) measurements were conducted using a PHI 5700 ESCA spectrometer with a monochromated Al Kα radiation ($h\nu$ = 1486.6 eV). Spectra correction was conducted using the C 1s line at 284.6 eV. Thermogravimetric analyses were performed to determine the mass percentage of MnO$_2$ in the MCN using a Pyris thermoanalyzer, on which 10 mg of the MCN sample was heated from 25 to 800 °C under an air flow rate of 100 ml min^{-1} and a temperature ramp of 10 °C min^{-1}. Nitrogen adsorption–desorption isotherms were measured at −196 °C on a Micromeritics ASAP 2010 apparatus. The specific surface area of samples was calculated by the Brunauer–Emmett–Teller (BET) equation, the total pore volume was determined at P/P_0 of 0.995, and the pore size distribution was estimated with adsorption branches based on the Barrett–Joyner–Halenda method. X-ray diffraction (XRD) patterns were collected with a D/Max-βb diffractometer using a Cu Kα radiation source (λ = 0.15432 nm). Transmission electron microscopy (TEM) images were obtained on a JEOL 2000EX electron microscope operating at an accelerating voltage of 120 kV. Prior to the observation, the samples were

ultrasonically dispersed in ethanol and then dropped onto carbon-coated copper grids.

3. Results and discussion

3.1. Characteristics of MCNs

Fig. 1 shows the typical SEM images of the PMMA colloidal crystal templates and the MCNs obtained by the CCTS. As shown in Fig. 1a, the PMMA template possessed a highly ordered array on a large area, although some individual defects could be observed. The surface of template was smooth and the average diameter of the PMMA microspheres was ~460 nm. Furthermore, the PMMA microspheres were arranged in a close-packed structure, with each sphere touching six others in the same layer. This meant that the PMMA colloidal crystals with high quality were obtained in our case, which was crucial to the final 3DOM products. When the different MP solutions were infiltrated into the interstices of the PMMA template arrays, the solutions could penetrate into the voids by capillary force. After drying out, they formed 3D skeleton in the templates, and 3DOM structure were finally achieved after thermal removal of the template and carbonization of P–F resol at high temperature. Fig. 1b–e illustrates the representative SEM images of the MCNs fabricated with different MPs. It was clearly observed that the samples B–D exhibited well developed interconnected networks of the ordered macropore structures. Meanwhile, it deserved to be mentioned that compared to the distorted and rambling 3DOM structures of the sample A obtained with MP-0 (Fig. 1b), the sample B, C or D derived from MP-1 (Fig. 1c), MP-2 (Fig. 1d) or MP-3 (Fig. 1e) respectively displayed a more intact and solid alignment of ordered macropores. The great enhancement on structure was probably due to the addition of $Mn(NO_3)_2$ in P–F resol, which led to form an appropriate precursor solution with a proper hydrolyzing or polymerizing speed. Such precursor solution facilitated the filling the voids in the template via a steady fluid-solid transformation [35,36].

Fig. 2 records the wide-angle XRD patterns of the samples A–D, one can only observe two broad peaks at around 23° which was typical of amorphous carbon materials [15–17]. No reflections corresponding to crystalline MnO_2 were observed, indicating that the MnO_2 in the nanocomposites were either amorphous or highly dispersed in the carbon framework.

XPS is an effective technique to determine the elements present and their chemical states (i.e. valence). Since it was unable to
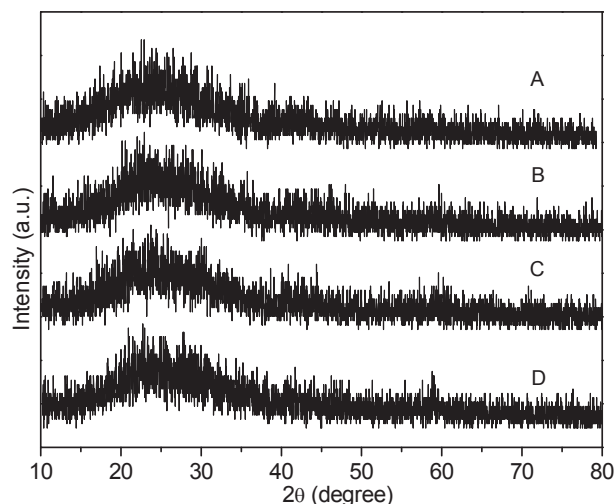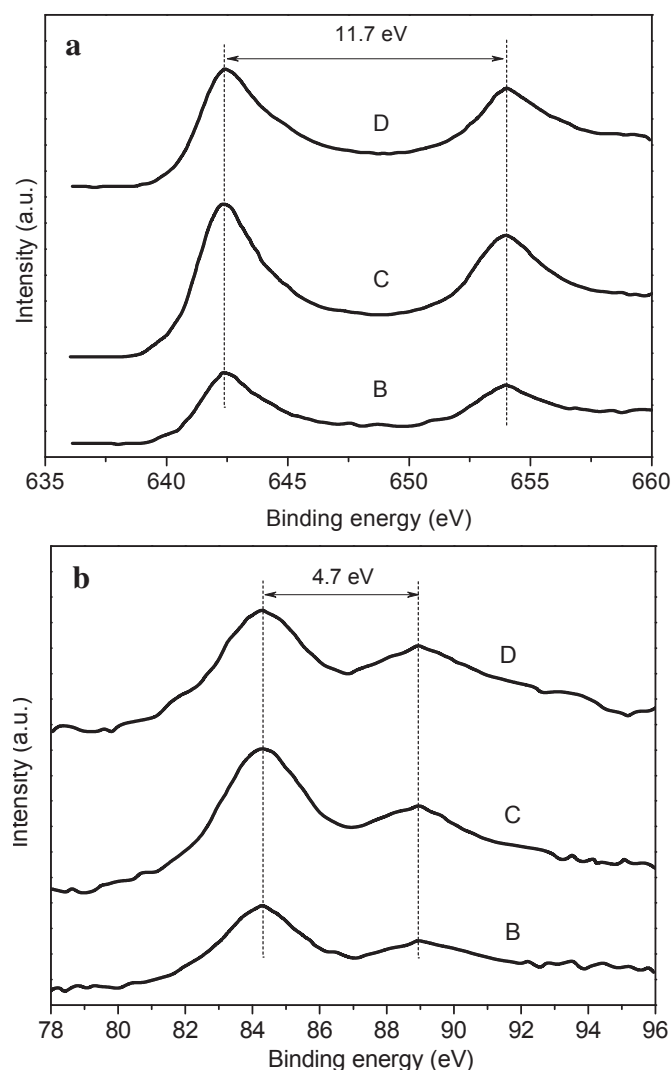
Fig. 3. XPS spectra of Mn 2p (a) and Mn 3s (b) of the samples B, C, and D.

identify the manganese valence information in the MCNs precisely by the XRD characterization, we conducted XPS to probe the chemical state of manganese atoms in the carbon framework. Fig. 3 depicts the XPS spectra of the samples B–D. It was clearly seen in Fig. 3a that for all the MCN samples, there were two peaks located at around 642.3 and 654.0 eV, respectively, which were attributed to the binding energies of Mn $2p_{3/2}$ and $2p_{1/2}$ with a spin-energy separation (ΔE_1) of 11.7 V, suggesting that the predominant manganese oxidation state is +4 [37]. On the other hand, it is well known that the oxidation state of manganese can also be determined from the peak separation (ΔE_2) of the doublet 3s peaks [38], which are originated from parallel spin coupling between electrons in the 3s and 3d orbits during the photoelectron ejection. The oxidation states of Mn increases with the decrease of ΔE_2 in an approximate linear relation [39,40]. As shown in Fig. 3b, the Mn 3s core level spectra presented two distinct peaks at 88.9 and 84.2 eV respectively for all the MCN samples. The corresponding ΔE_2 was 4.7 eV, which was similar to the reported results expected for Mn 4+ [41,42]. Based on the XPS analyses, it was concluded that the element manganese in the MCN samples existed in the chemical state of Mn(IV). In addition, an increase in intensity for both Mn_{2p} and Mn_{3s} was seen, demonstrating the increasing MnO_2 content in the MCNs.

Fig. 2. XRD patterns of the samples A, B, C, and D.

Fig. 4a exhibits the N_2 adsorption–desorption isotherms of the samples A–D. It was found that all the isotherms belonged to a mixed type corresponding to macropores with certain meso- and micropores, which exhibited a type II isotherm with an H3-type hysteresis loop and three N_2 uptake phases. Below the very low relative pressure of $P/P_0 = 0.1$, there was a significant quick rise of adsorption branch, indicating the presence of some micropores generated possibly from the carbonization of P–F resol. With the increase of the relative pressure from $P/P_0 = 0.1$ to $P/P_0 = 0.8$, the N_2 adsorption amounts increased gradually accompanying with a slight H2-type hysteresis loop related to the capillary condensation taking place, implying the existence of some mesopores of a variety of sizes. At high relative pressures of $P/P_0 = 0.8$–1.0, an obvious H3-type hysteresis loop, which had no clear adsorption plateau at $P/P_0 \approx 1.0$, indicative of a macroporous size distribution, was observed. Such a phenomenon was also observed in the others surfactants-assisted preparation of 3DOM materials [43–50], feature of combination of macro-mesopore structure. According to BJH adsorption curves, the average mesopore sizes of the samples A-D were centered in the range of 2.3–2.6 nm (Fig. 4b), suggesting that introduction of different amount of $Mn(NO_3)_2$ to the MP had little influence on the size of mesopores. Table 2 lists the textural properties of the samples A–D. With increasing MnO_2 content in

Table 2
Textural properties of the MCN samples.

Sample	S_{BET} (m^2 g^{-1})	S_{meso} (m^2 g^{-1})	S_{mic}(m^2 g^{-1})	V_p (cm^3 g^{-1})	MnO_2 content (wt.%)
A	935	663	255	0.71	0.0
B	928	658	251	0.70	6.5
C	916	659	247	0.68	12.6
D	906	653	246	0.67	21.3

the samples A–D, the BET surface area (S_{BET}) decreased slightly from 935 m^2 g^{-1} for sample A, to 928 m^2 g^{-1} for sample B, 916 m^2 g^{-1} for sample C, and 906 m^2 g^{-1} for sample D. Similarly, the total pore volumes (V_p) were also found to decrease slightly from 0.71 to 0.67 cm^3 g^{-1} with increasing in MnO_2 content. This was likely stemmed from minimal part of pore blocking by MnO_2. The negligible mesoporous surface areas (S_{meso}) and microporous surface areas (S_{mic}) changes, almost remaining constant (S_{meso} = 660 m^2 g^{-1} and S_{mic} = 250 m^2 g^{-1}), also implied that the MnO_2 nanoparticles did not form in the mesopores of the carbon.

Fig. 5 presents the representative TEM images of the sample D at different magnification. The interconnected networks of 3DOM structures with overlapped pores could be clearly observed in Fig. 5a, confirming the well defined three-dimensionally ordered structure of the sample D. On the other hand, the partial magnified image in Fig. 5b showed that MnO_2 nanoparticles were highly distributed on the macropore walls of the 3DOM carbon scaffold. The sizes of MnO_2 nanoparticles fell in the range of 2–6 nm, as seen by the black spots, proving the presumption of XRD characterization. No bulk aggregates of MnO_2 were found on the 3DOM carbon scaffold. In addition, there were numerous mesopores or nanovoids with sizes in the range of subnanometer (less than 1 nm) to 5 nm randomly distributed in the macropore walls of the 3DOM carbon scaffold. The emergence of mesopores or nanovoids was attributed to the templating function of F127, which potentially contributed to the enhancement in surface area. This was well consistent with N_2-sorption results.

3.2. Electrochemical performances

The synthesis of 3DOM MCNs with a hierarchically porous network and uniform composition affords a promising electrode material for enhancing performance of manganese oxide-based electrochemical supercapacitors. The electrochemical properties of the 3DOM MCN electrodes were examined by CV and GCD tests. Fig. 6a shows the CV curves of the 3DOM MCN electrodes in 0.1 M Na_2SO_4 as a function of mass percentage of MnO_2 in the 3DOM MCN electrode at a scan rate of 50 mV s^{-1}. The potential window for cycling was confined between 0 and 0.8 V versus SCE to avoid the oxygen evolution reaction at higher potential and MnO_2 dissolution at lower potentials [51]. It was clearly seen that the CV profiles exhibited nearly symmetrical rectangular shapes in potential window, which were ideal capacitive behaviors involving two types of capacitive contributing from electric double-layer capacitance (EDLC) generated from the 3DOM carbon substrate and pseudo-capacitance from MnO_2 [52,53]. There were no distinct redox peaks on the CV curves for the samples. Gogotsi et al. proposed that the fast, reversible successive surface redox reactions within the voltage window defined the behavior of the voltammogram, whose shape was close to that of the EDLC [54]. In addition, the hierarchical pore structure and uniform framework composition of the 3DOM MCN electrodes contributed the ideal capacitive behaviors. The 3DOM carbon electrode (sample A in Fig. 6a) possessed a current density of ~0.06 mA cm^{-2} based on EDLC, indicating a lower capacitance in neutral aqueous electrolyte than in other medium
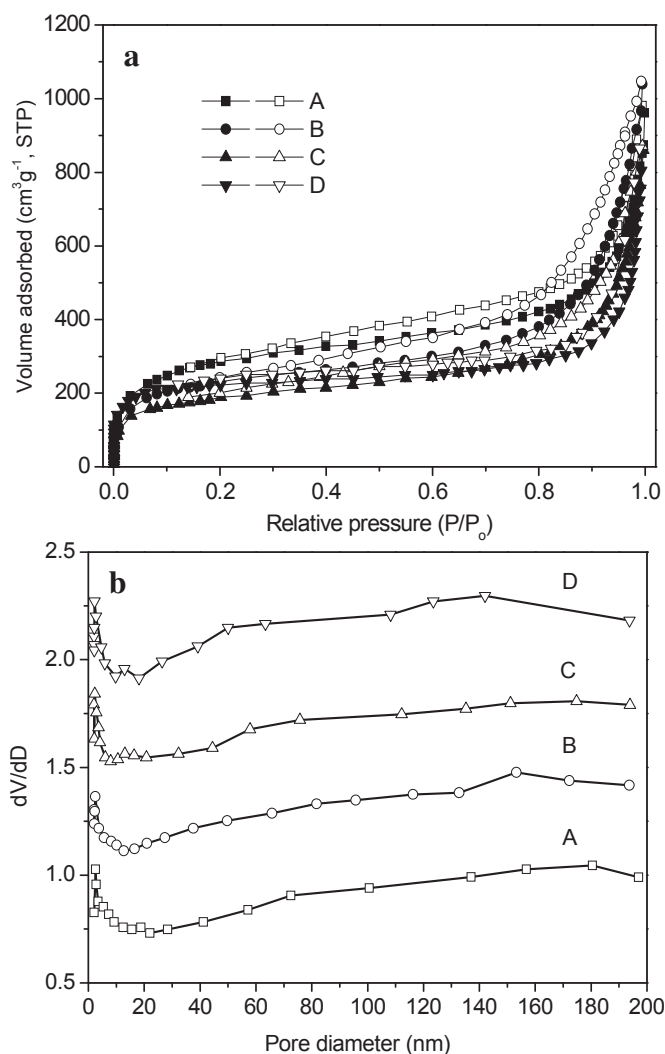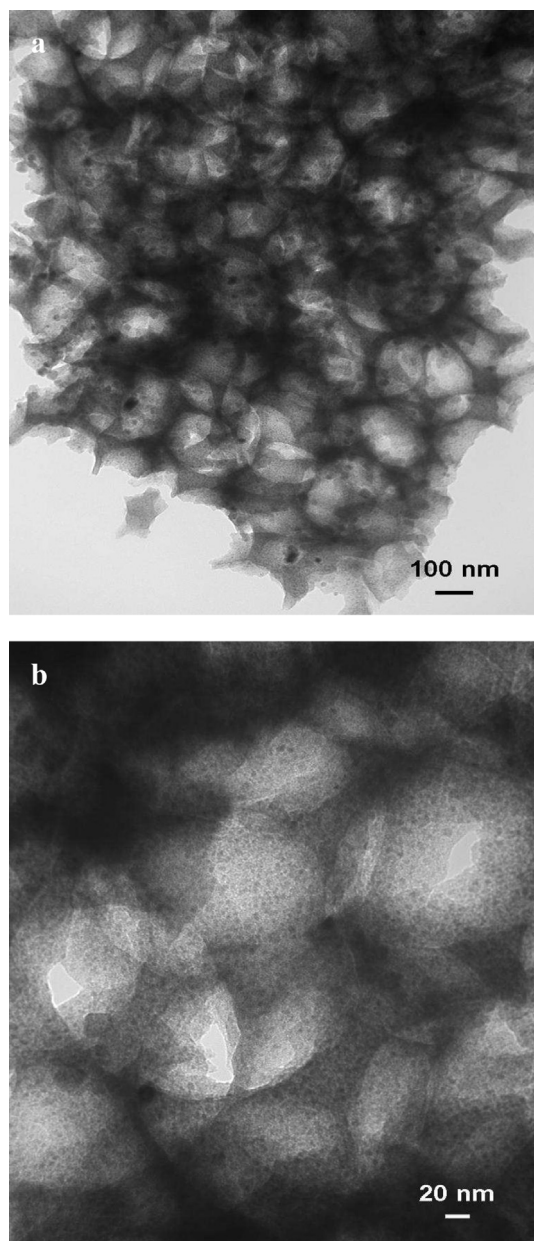

Fig. 4. Nitrogen adsorption–desorption isotherms (a) and corresponding pore size distributions (b) of the samples A–D.

Fig. 5. TEM images of the representative sample D at low (a) and high (b) magnification.

densities with the scan rates and nearly rectangular shapes, indicating the fast charge/discharge process characteristic. Generally, it is believed that the slow diffusion of ions in the electrode will lead to a nonideal rectangular shape of CV curve at a high scan rate [54]. In our case, the sample D with hierarchical pore structure can overcome this disadvantage. First, interconnected 3DOM carbon in the MCN not only acts as the support for the dispersion of MnO_2 nanoparticles but also provides a fast ion transportation pathway for the electrolyte to reach the active surface of MnO_2. Its hierarchical mesopores and/or nanovoids in the walls favor fast diffusion of electrolyte ions into the pores, formation of EDLCs, and thus leading to higher capacitance [57,58]. Second, nanoscale size of MnO_2 particles (2–6 nm) can greatly reduce the diffusion length over which Na^+ must transfer during the charge/discharge process, thus improving the electrochemical utilization of MnO_2. Last, in the present CCTS, the manganese precursor containing $Mn(NO_3)_2$ and P–F resol can be directly introduced into the 3D PMMA template. After pyrolysis, the resulting 3DOM MCN not only yields intimate contact and strong interaction between the MnO_2 and the 3DOM carbon matrix, but it also makes the MnO_2 highly dispersed in the 3DOM carbon matrix, which are of great benefit to fast
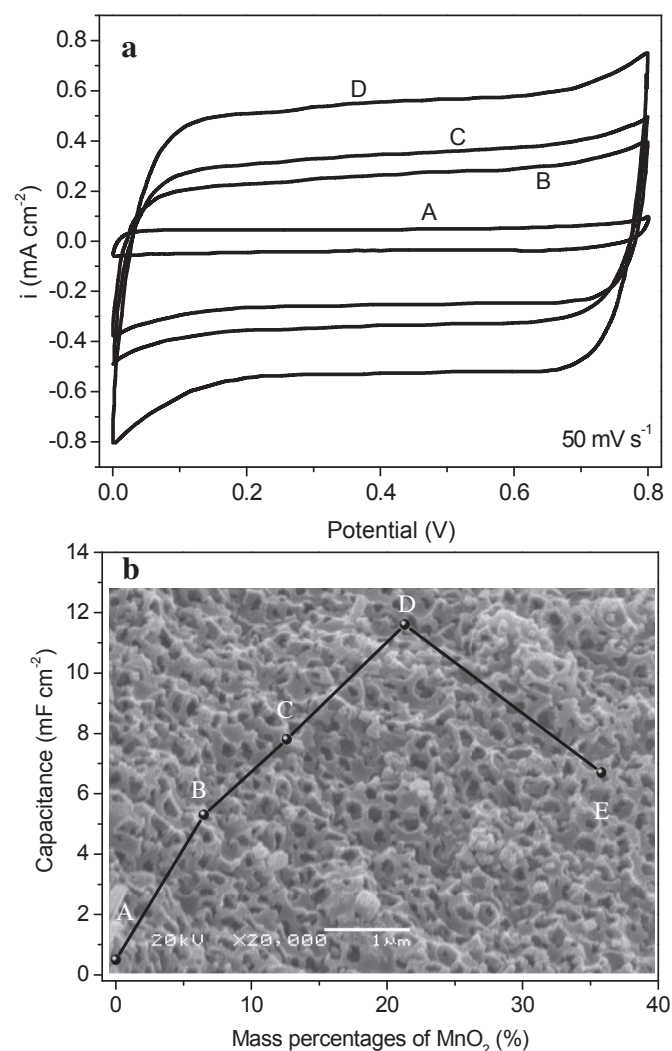
Fig. 6. Cycle voltammograms for the 3DOM MCN electrodes in 0.1 M Na_2SO_4 (a) and areal capacitance as a function of mass percentages of MnO_2 with a scan rate of 50 mV s^{-1} (b), the inset is the corresponding SEM image of MCN with a MnO_2 content of 35.8 wt.%.

[55,56]. Because of the incremental MnO_2 pseudocapacitive contribution to the overall capacitance, the current density remarkably increased from sample B to sample D with the increasing MnO_2 content. A maximum areal capacitance of 11.6 mF cm^{-2} was achieved for the sample D. Further increase of MnO_2 content to 35.8 wt.% (denoted as sample E) led to a striking decrease of areal capacitance to 6.7 mF cm^{-2} due to the severe distortion of the resulting 3DOM structure (SEM inset of Fig. 6b) and the much more suppression of pseudocapacitance in MnO_2 with low electrical conductivity. Evidently, the sample D might be the most appealing candidate for the electrode material for supercapacitor applications.
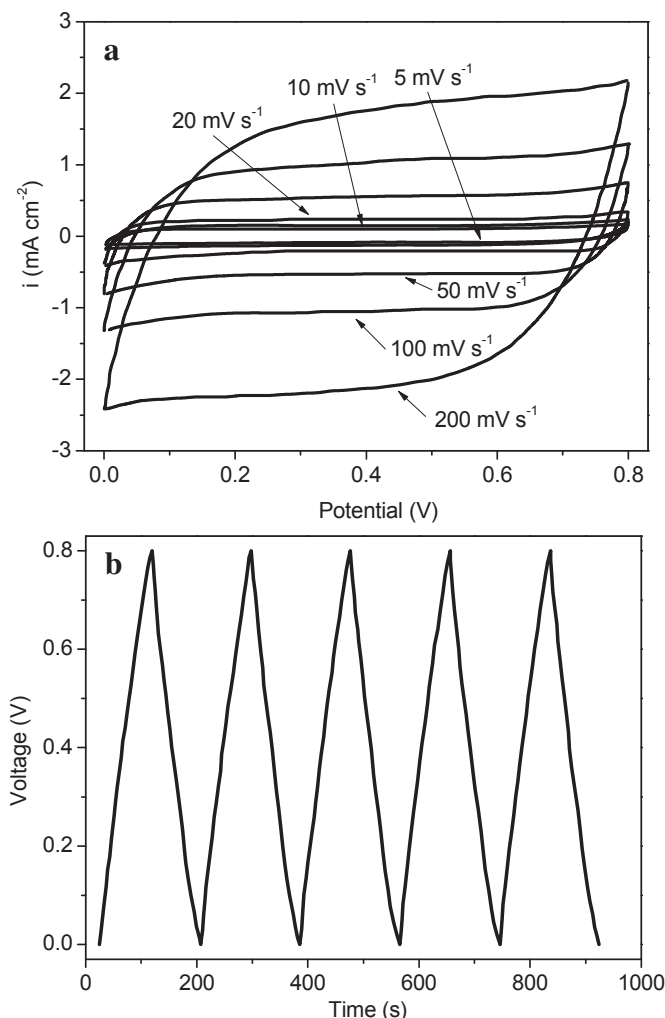
Fig. 7a exhibits the CV curves of the sample D electrode at scan rates over the range of 5–200 mV s^{-1} with potential windows ranging from 0 to 0.8 V versus SCE in 0.1 M Na_2SO_4 aqueous solution. It was well observed that these CV curves showed increasing

Fig. 7. Cyclic voltammograms for the sample D electrode at scan rates from 5 to 200 mV s^{-1} (a) and galvanostatic charge/discharge curves of the sample D electrode at a constant current density 1 A g^{-1} (b).

specific capacitance of MnO$_2$, the 3DOM MCN (sample D), and pure 3DOM carbon (sample A), respectively. C% and Mn% indicate the weight percentages of C and MnO$_2$ in the sample D, respectively. The specific capacitance of pure 3DOM carbon was about 122 F g^{-1}. The corresponding specific capacitance of MnO$_2$ in the sample D was calculated as 1178 F g^{-1}, approaching the theoretical value of MnO$_2$ (1370 F g^{-1}). As the current density increased from 0.5 to 10 A g^{-1}, the sample D electrode preserved 67.7% of its initial specific capacitance from 347 to 235 F g^{-1}, suggesting a high retention of specific capacitance of the sample D electrode.

In order to further understand the GCD results, EIS was used to quantify the conductive and diffusive behavior of the 3DOM MCN electrodes. Fig. 9 records Nyquist plots of the 3DOM MCN electrodes with different MnO$_2$ content (samples B to D). It was noted that all of the electrodes had a comparable ohmic resistance with a single semicircle in the high frequency region and a straight line in the low frequency region. The polarization resistance (R_p), shown in the high frequency region, increased gradually as the MnO$_2$ content was increased. The sample D electrode had an R_p of ~4.1 Ω calculated from the diameter of the semicircle, which was higher than that of the samples B (~1.4 Ω) and C (~2.5 Ω) electrodes. It is assumed that a bulk resistivity of MnO$_2$ is around 5×10^5 Ω cm^{-1}, a pure MnO$_2$ electrode with a thickness of only ~2 μm as the electrode will have a resistance of ~100 Ω [59]. Apparently, the 3DOM carbon framework in the MCNs did serve as an effective conductive pathway, dramatically reducing the resistance. On the other hand, with the increasing MnO$_2$ content, the slope of the Nyquist plot in the low frequency region decreased gradually, indicative of the increasing Warburg resistance (or diffusion resistance). These results were in good agreement with the CV and GCD results, verifying that higher MnO$_2$ content led to larger charge transfer resistance and diffusion resistance. Therefore, in order to achieve good capacitance performance for the 3DOM MCN electrodes, it is crucial to maintain a connective carbon framework with good conductivity and introduce a rational MnO$_2$ content for high specific capacitance.

Long cycle durability is an important merit for supercapacitors. Fig. 10a indicates the cycle life of the sample D electrode measured by the consecutive GCD at a current density of 2.5 A g^{-1}. It was seen that the curve demonstrated a stable 3DOM MCN electrode with only less than 8% decay (92.3% retention) in specific capacitance
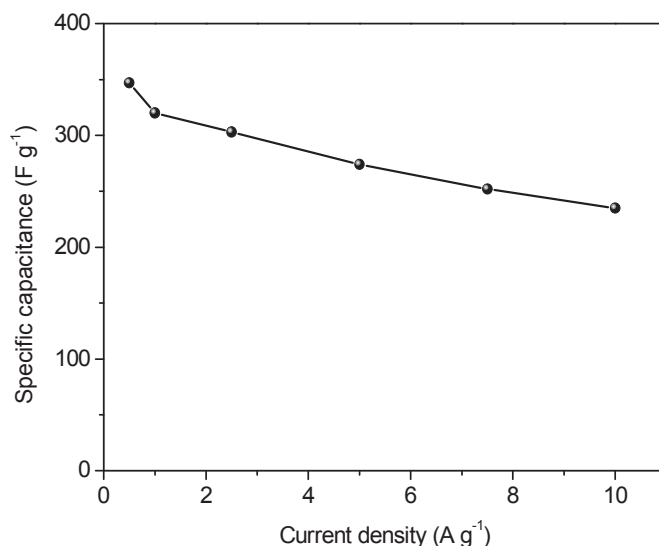
transportation of electron throughout the whole electrode matrix. Therefore, the curve still retained a rectangular shape even at a high scan rate of 200 mV s^{-1}, implying the electrode had ideal capacitive behavior and high-rate performance. Fig. 7b exhibits the GCD curve of the sample D at a current density of 1 A g^{-1}. It was noted that the charge/discharge cycles were very stable. The charging curves were near straight and very symmetric with the corresponding discharging counterparts, which also indicated a good electrochemical capacitive characteristic with the coulomb efficiencies closing to 100%. This result was well consistent with that of the CV testing.

Current density is an important factor influencing the power behavior of supercapacitor. For further evaluating the rate capability of the sample D electrode, GCD measurements were further carried out at different current densities. The specific capacitances of the electrode are calculated as $C = I \times \Delta t / m \times \Delta v$ (three-electrode system), where I is the discharge current (A), Δt is the discharge time (s), m is the mass of the total electrode materials (g), and ΔV is the potential difference (V) during the discharging, respectively. Fig. 8 shows the variation in specific capacitances of the sample D electrode at different current densities. It was observed that the sample D electrode possessed a specific capacitance of 347 F g^{-1} when the current density was 0.5 A g^{-1}. According to the equation, $C_{Mn} = (C_{MCN} - C_C C\%)/Mn\%$, where C_{Mn}, C_{MCN}, and C_C represent the

Fig. 8. Variation of specific capacitance for the sample D electrode at a current density from 0.5 to 10 A g^{-1}.
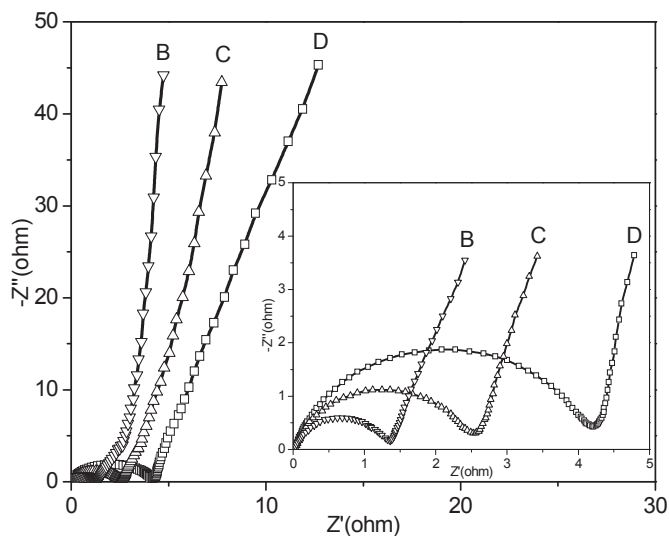
Fig. 9. Nyquist plots of the samples B, C and D electrodes.

after 5500 cycling. After 5500 cycling, the 3DOM structure of the sample D was still maintained with partial pore distortion and damage to some extent, and the whole structural integrity of active electrode materials remained considerably, as shown in Fig. 10b,
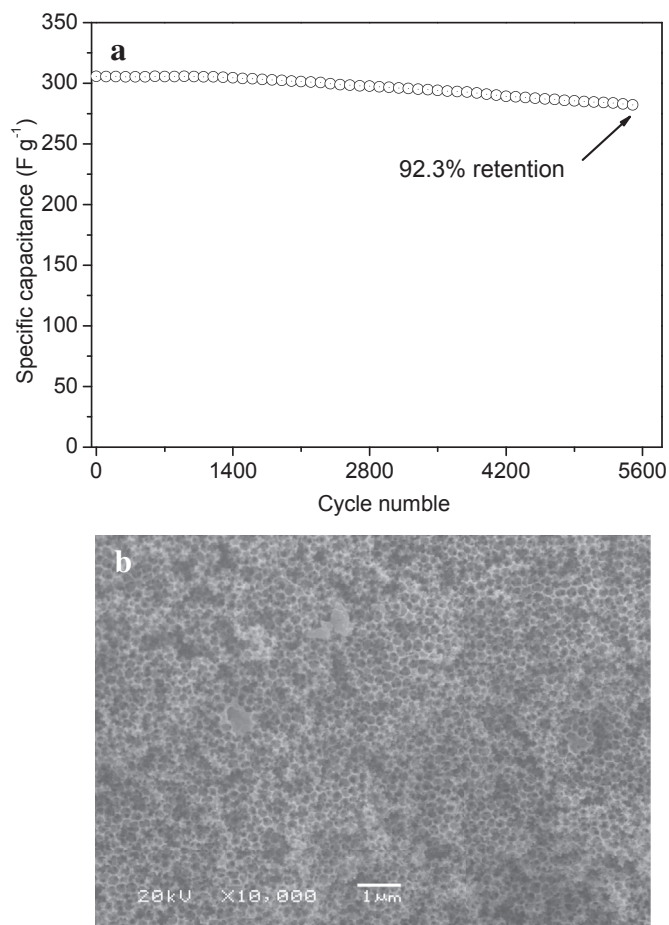

Fig. 10. Capacitance retention of the sample D electrode as a function of cycle number at a current density of 2.5 A g^{-1} (a), SEM image of the sample D electrode after completing 5500 charge/discharge cycling (b).

indicating that the long-term repeating charge/discharge operation did not completely spoil the structure of the sample D electrode and the specific capacitance could be well preserved.

4. Conclusions

In this work, we have prepared the 3DOM MCN with hierarchical pore structure and uniform composition of MnO$_2$ and carbon by the CCTS. The resulting nanocomposite combined the essential properties of the carbon substrate and the pseudoactive of MnO$_2$. The electrochemical measurements showed that the nanocomposite electrode possessed a high specific capacitance of 347 F g^{-1}, an excellent rate capability with specific capacitance preserved 67.7% with current density increasing from 0.5 to 10 A g^{-1} and good cycling performance of 92.3% retention after 5500 cycles. Such superior capacitive performance can be attributed to the following synergetic contributions of the 3DOM MCN electrode: (i) facilitating rapid ion transportation pathway throughout the 3DOM channels, (ii) ensuring much higher electrolyte flux across the electrode due to the dramatically increased electrode–electrolyte interface, (iii) providing good mechanical stability and high surface area to maximize the capacitance. (iv) Highly dispersed MnO$_2$ nanoparticles on the 3DOM carbon substrate, providing the main pseudocapacitance, increasing the electrochemical utilization of MnO$_2$ pseudocapacity, and enabling the fast electron transfer within electrode. These results should deepen the understanding of the role of combining hierarchical ordered macrostructure with MnO$_2$ in supercapacitor. Such a simple synthetic procedure may be a versatile approach that can be extended to the fabrication of some other manganese oxide–carbon nanocomposites for supercapacitor and is worthy of further exploration.

Acknowledgments

References

[1] G.P. Wang, L. Zhang, J.J. Zhang, Chem. Soc. Rev. 41 (2012) 797–828.
[2] M.J. Zhi, C.C. Xiang, J.T. Li, M. Li, N.Q. Wu, Nanoscale 5 (2013) 72–88.
[3] X. Zhang, X.Z. Sun, H.T. Zhang, D.C. Zhang, Y.W. Ma, Mater. Chem. Phys. 137 (2012) 290–296.
[4] M.J. Kim, Y.S. Hwang, K.C. Min, J.H. Kim, Electrochim. Acta 113 (2013) 322–331.
[5] S.L. Chou, J.Z. Wang, S.Y. Chew, H.K. Liu, S.X. Dou, Electrochem. Commun. 10 (2008) 1724–1727.
[6] J. Yan, Z.J. Fan, T. We, J. Cheng, B. Shao, K. Wang, L.P. Song, M.L. Zhang, J. Power Sources 194 (2009) 1202–1207.
[7] L.B. Hu, W. Chen, X. Xie, N. Liu, Y. Yang, H. Wu, Y. Yao, M. Pasta, H.N. Alshareef, Y. Cui, ACS Nano 5 (2011) 8904–8913.
[8] H.J. Zheng, J.X. Wang, Y. Jia, C.A. Ma, J. Power Sources 216 (2012) 508–514.
[9] S. Chen, J.W. Zhu, X.D. Wu, Q.F. Han, X. Wang, ACS Nano 4 (2010) 2822–2830.
[10] Q. Cheng, J. Tang, J. Ma, H. Zhang, N. Shinya, L.C. Qin, Carbon 49 (2011) 2917–2925.
[11] Z.B. Lei, F.H. Shi, L. Lu, ACS Appl. Mater. Interfaces 4 (2012) 1058–1064.
[12] Y.J. Yang, E.H. Liu, L.M. Li, Z.Z. Huang, H.J. Shen, X.X. Xiang, J. Alloys Compd. 487 (2009) 564–567.
[13] M.N. Patel, X.Q. Wang, D.A. Slanac, D.A. Ferrer, S. Dai, K.P. Johnston, K.J. Stevenson, Mater. Chem. 22 (2012) 3160–3169.
[14] Y.C. Chen, Y.K. Hsu, Y.G. Lin, Y.K. Lin, Y.Y. Horng, L.C. Chen, K.H. Chen, Electrochim. Acta 56 (2011) 7124–7130.
[15] S.M. Zhu, H.S. Zhou, M. Hibino, I. Honma, M. Ichihara, Adv. Funct. Mater. 15 (2005) 381–386.
[16] X.P. Dong, W.H. Shen, J.L. Gu, L.M. Xiong, Y.F. Zhu, H. Li, J.L. Shi, Microporous Mesoporous Mater. 91 (2006) 120–127.
[17] X.P. Dong, W.H. Shen, J.L. Gu, L.M. Xiong, Y.F. Zhu, H. Li, J.L. Shi, J. Phys. Chem. B 110 (2006) 6015–6019.
[18] A.E. Fischer, K.A. Pettigrew, D.R. Rolison, R.M. Stroud, J.W. Long, Nano Lett. 7 (2007) 281–286.

[19] G.R. Li, Z.P. Feng, Y.N. Ou, D.C. Wu, R.W. Fu, Y.X. Tong, Langmuir 26 (2010) 2209–2213.
[20] A. Vu, A. Stein, Chem. Mater. 23 (2011) 3237–3245.
[21] M. Sadakane, R. Kato, T. Murayama, W. Ueda, J. Solid State Chem. 184 (2011) 2299–2305.
[22] Z. Liu, Y. Yang, J.H. Mi, X.L. Tan, C. Lv, Int. J. Hydrogen Energy 38 (2013) 4445–4455.
[23] I. Moriguchi, F. Nakahara, H. Furukawa, H. Yamada, T. Kudo, Electrochem. Solid State Lett. 7 (2004) A221–A223.
[24] S. Tabata, Y. Isshiki, M. Watanabe, J. Electrochem. Soc. 155 (2008) K42–K49.
[25] H. Yamada, I. Moriguchi, T. Kudo, J. Power Sources 175 (2008) 651–656.
[26] S.W. Woo, K. Dokko, H. Nakano, K. Kanamura, J. Mater. Chem. 18 (2008) 1674–1680.
[27] S.W. Woo, K. Dokko, K. Kanamura, J. Power Sources 185 (2008) 1589–1593.
[28] S.W. Woo, K. Dokko, H. Nakano, K. Kanamura, J. Power Sources 190 (2009) 596–600.
[29] L.L. Zhang, S. Li, J.T. Zhang, P.Z. Guo, J.T. Zheng, X.S. Zhao, Chem. Mater. 22 (2010) 1195–1202.
[30] H. Nishihara, T. Kyotani, Adv. Mater. 24 (2012) 4473–4498.
[31] Z. Liu, J.H. Mi, Y. Yang, X.L. Tan, C. Lv, Electrochim. Acta 115 (2014) 206–215.
[32] M.A. Al-Daous, A. Stein, Chem. Mater. 15 (2003) 2638–2645.
[33] L.J. Fu, T. Zhang, Q. Cao, H.P. Zhang, Y.P. Wu, Electrochem. Commun. 9 (2007) 2140–2144.
[34] Y. Meng, D. Gu, F.Q. Zhang, Y.F. Shi, H.F. Yang, Z. Li, C.Z. Yu, B. Tu, D.Y. Zhao, Angew. Chem. Int. Ed. 44 (2005) 7053–7059.
[35] H.W. Yan, C.F. Blanford, B.T. Holland, W.H. Smyrl, A. Stein, Chem. Mater. 11 (1999) 795–805.
[36] H.W. Yan, C.F. Blanford, B.T. Holland, W.H. Smyrl, A. Stein, Chem. Mater. 12 (2000) 1134–1141.
[37] C.D. Wanger, W.M. Riggs, L.E. Davis, J.F. Moulder, G.E. Muilenberg, Handbook of X-ray Photoelectron Spectroscopy, Perkin–Elmer, Eden Prairie, 1978.
[38] T. Tomko, R. Rajagopalan, M. Lanagan, H.C. Foley, J. Power Sources 196 (2011) 2380–2386.
[39] B. Djurfors, J.N. Broughton, M.J. Brett, D.G. Ivey, Acta Mater. 53 (2005) 957–965.
[40] X.J. Wang, H.M. Liu, X. Chen, D.G. Evans, W.S. Yang, Electrochim. Acta 78 (2012) 115–121.
[41] W. Wei, X. Cui, W. Chen, D.G. Ivey, J. Power Sources 186 (2009) 543–550.
[42] L.J. Sun, X.X. Liu, Eur. Polym. J. 44 (2008) 219–224.
[43] R.Z. Zhang, H.X. Dai, Y.C. Du, L. Zhang, J.G. Deng, Y.S. Xia, Z.X. Zhao, X. Meng, Y.X. Liu, Inorg. Chem. 50 (2011) 2534–2544.
[44] H. Zhang, H.X. Dai, Y.X. Liu, J.G. Deng, L. Zhang, K.M. Ji, Mater. Chem. Phys. 129 (2011) 586–593.
[45] J.Q. Zhao, P. Wan, J. Xiang, T. Tong, L. Dong, Z.N. Gao, X.Y. Shen, H. Tong, Microporous Mesoporous Mater. 138 (2011) 200–206.
[46] Y.X. Liu, H.X. Dai, Y.C. Du, J.G. Deng, L. Zhang, Z.X. Zhao, C.T. Au, J. Catal. 287 (2012) 149–160.
[47] Z.X. Zhao, H.X. Dai, J.G. Deng, Y.C. Du, Y.X. Liu, L. Zhang, Microporous Mesoporous Mater. 163 (2012) 131–139.
[48] D.Z. Han, X. Li, L. Zhang, Y.H. Wang, Z.F. Yan, S.M. Liu, Microporous Mesoporous Mater. 158 (2012) 1–6.
[49] H. Arandiyan, H.X. Dai, J.G. Deng, Y.X. Liu, B.Y. Bai, Y. Wang, X.W. Li, S.H. Xie, J.H. Li, J. Catal. 307 (2013) 327–339.
[50] Y.C. Wei, Z. Zhao, T. Li, J. Liu, A.J. Duan, G.Y. Jiang, Appl. Catal. B 146 (2014) 57–70.
[51] T. Brousse, P.L. Taberna, O. Crosnier, R. Dugas, P. Guillemet, Y. Scudeller, Y. Zhou, F. Favier, D. Bélanger, P. Simon, J. Power Sources 173 (2007) 633–641.
[52] H. Pan, J.Y. Li, Y.P. Feng, Nanoscale Res. Lett. 5 (2010) 654–668.
[53] W. Wei, X. Cui, W. Chen, D.G. Ivey, Chem. Soc. Rev. 40 (2011) 1697–1721.
[54] P. Simon, Y. Gogotsi, Nat. Mater. 7 (2008) 845–854.
[55] V. Subramanian, H.W. Zhu, B.Q. Wei, Electrochem. Commun. 8 (2006) 827–832.
[56] X. Xie, L. Gao, Carbon 45 (2007) 2365–2373.
[57] K.S. Xia, Q.M. Gao, J.H. Jiang, J. Hu, Carbon 46 (2008) 1718–1726.
[58] W. Xing, C.C. Huang, S.P. Zhuo, X. Yuana, G.Q. Wang, D. Hulicova-Jurcakova, Z.F. Yan, G.Q. Lu, Carbon 47 (2009) 1715–1722.
[59] R.N.D. Guzman, A. Awaluddin, Y. Shen, Z. Tian, S.L. Suib, S. Ching, C. O'Young, Chem. Mater. 7 (1995) 1286–1292.